physica status solidi rrl
www.pss-rapid.com

3D Nanostructured Electrodes Based on Anodic Alumina Templates for Stable Pseudocapacitors

Tabish Aftab, Osbel Almora, Josep Ferre-Borrull,* and Lluis F. Marsal*

This study investigates the preparation of nickel nanostructured electrodes for the enhancement of supercapacitor performance. The nanostructured electrodes are synthesized using nanoporous anodic alumina (NAA) as a template via the pulsed electrodeposition method. Structural properties are examined using field-emission scanning electron microscopy, while electrochemical characterization is conducted through cyclic voltammetry (CV) and electrochemical impedance spectroscopy. The results reveal that Ni nanorod arrays can be obtained embedded in the NAA matrix and with electrical contact with the aluminum substrate. On average, the rods are spaced 90 nm apart, with a diameter of 70 nm and a length of 2 μm. The Ni@NAA electrode exhibits an enlarged active area and exceptional electrochemical performance, demonstrating remarkable stability over 5000 cycles of CV at a scan rate of 50 mV s^{-1}. Specific capacitance values exceeding 100 mF cm^{-2} and maximum charging times of less than 10 min are reported, highlighting its suitability for high-power energy devices requiring pseudo-supercapacitance. The study underscores the significance of nanostructured electrodes in advancing energy storage technologies and presents promising prospects for practical applications.

1. Introduction

In recent years, there has been significant attention on the energy sector, especially when it comes to the exploration of various alternative energy storage sources. Among these advancements, supercapacitors (SCs) have emerged as an extremely promising technology due to their exceptional storage capabilities, rapid charging–discharging ability, and prolonged lifespan.[1–4] SCs differ from batteries in a fundamental way: instead of relying on a chemical process to store electrical charge, they directly accumulate it on the surface of an active material through electrostatic means. The so-called electrochemical capacitors typically operate by utilizing the electrochemical double-layer capacitance (EDLC) that develops at the interface between an electrode and an electrolyte.[5] EDLC devices exhibit an impressive ability to rapidly charge and discharge across multiple cycles. This remarkable feature stems from their unique charge storage mechanism, resulting in a high-power density.[6] However, their energy density is constrained by the size of their effective double-layer surface. On the other hand, pseudocapacitors, namely, capacitors based on transition metal oxide/hydroxide, have the ability to store charge through redox reactions occurring at or near the surface of their electrode materials.[7] These capacitors have a larger capacitance, but their charge and discharge are not as quick as those with EDLC and have poor long-term stability.

The performance of SCs has been enhanced in recent years through the integration of carbon-based materials (such as carbon nanotubes, graphene, and graphite nanoparticles),[8] metallic composite materials,[9] metal–polymer composite materials,[10] pseudocapacitive materials,[11] etc. However, utilization of SCs in large-scale energy storage systems is still restricted due to their poor energy density. Constructing an advanced pseudo-SC with both high energy density and exceptionally long lifespans remains a challenge in the field of advanced energy storage technologies. While it is true that increasing the active area of electrode materials typically leads to higher specific capacitance, practical devices often experience a decrease in specific capacitance due to the higher resistance of the electrode material.[12] Furthermore, when the electrodes undergo electrochemical reactions, their mass and volume may change significantly causing strain on the structure that can lead to the creation of cracks or the pulverization of active materials.

Making a nanostructured electrode is a promising solution to create a larger active area and empty spaces (to accommodate volume change), resulting in a significant increase in capacitance and cycling performance. The increase in surface area of the electrode allows more ions to interact, leading to higher specific capacitance. Prior studies have documented the successful application of pseudocapacitive materials (such as metal oxides,[13] sulfides,[14] and layered double hydroxides)[15] onto nanostructured surfaces to create hierarchical (layered) electrodes. For instance, nickel oxide nanotubes and nanoporous electrodes have been demonstrated for SC applications. These electrodes demonstrate enhanced specific capacity, higher power density, and cycling stability. However, maintaining an outstanding performance of hierarchical electrodes remains challenging due to their substantial electrode mass. Given the aforementioned

T. Aftab, O. Almora, J. Ferre-Borrull, L. F. Marsal
Departament d'Enginyeria Electrònica
Elèctrica i Automàtica
Universitat Rovira i Virgili
Avinguda Paisos Catalans, 26, 43007 Tarragona, Spain
E-mail: osbel.almora@urv.cat; josep.ferre@urv.cat

The ORCID identification number(s) for the author(s) of this article can be found under https://doi.org/10.1002/pssr.202400144.

DOI: 10.1002/pssr.202400144

factors, it is imperative to study the function of nanostructured electrodes in enhancing the energy storage capacity of SCs, particularly in relation to the materials used for current collectors.

In this study, we utilized nickel to create a metallic nanostructured electrode, as opposed to using hierarchical material electrodes or conformal coatings.[16] Ni exhibits excellent electrical conductivity and has been utilized as a component in composite/hierarchical materials to create nanostructured electrodes. Also, Ni possesses pseudocapacitance characteristics when utilized as an electrode, and nickel oxide nanotubes[17] and nanoporous films[18,19] have been demonstrated for SC applications. However, to the best of our knowledge, its potential as a nanostructured electrode with nanoporous alumina template has yet not been explored. Herein, we present a method for synthesizing metallic nanostructured electrodes using nanoporous anodic alumina (NAA) as a template. The electrodes were prepared through the pulsed electrodeposition method. Additionally, we have examined the structural properties of as-prepared nanostructured electrode by field-emission scanning electron microscopy (FESEM) and conducted electrochemical characterization on the basis of cyclic voltammetry (CV) and electrochemical impedance spectroscopy (EIS). The detailed results are presented and discussed.

2. Results and Discussion

The structural morphology and pore structure of the Ni@NAA at different stages of production were studied using FESEM. **Figure 1**a shows the top-view SEM picture of a sample obtained after the two-step anodization and barrier layer removal processes. It can be observed that the average pore diameter is around 70 ± 5 nm and the average interpore distance is 90 nm (see Figure S2, Supporting Information). The pores appear ordered in a triangular lattice at the scale of the picture. Figure 1b corresponds to a sample after the nickel pulsed electrodeposition (for pictorial image, refer Figure S3, Supporting Information). The picture shows the same pore structure as in (a), although the insides of pores appear with different shades of gray. The different shades of gray indicate that nickel is filling the pores up to different levels, the brighter pores corresponding to a higher level of filling. It is remarkable that no pore appears to be overfilled. It should be noted that pore diameters and pore wall thicknesses are not modified during the nickel deposition. Figure 1c shows the top view of a sample after the pore wall thinning process. The thinning of the pore walls reveals the curved surface of the nanorods, thus providing a volume for the electrolyte to fill and a big active area of the nickel nanorods to react with the electrolyte. Figure 1d shows a cross-sectional view of a sample obtained in the same conditions as in (c). The nickel nanorods and their contact with the base aluminum can be observed. The bottom of the nanorods appears branched, a characteristic of the barrier layer thinning process. The length of the rods is estimated to be around 2 μm and the diameter of around 70 nm (see Figure S4 and S5, Supporting Information). The remains of some of the oxide pore walls can also be seen in the picture as a relatively darker ring encircling the brighter nanorods (see Figure S6, Supporting Information).

CV measurements were performed to analyze the operation of the Ni@NAA electrodes using a three-electrode cell in a 1 M

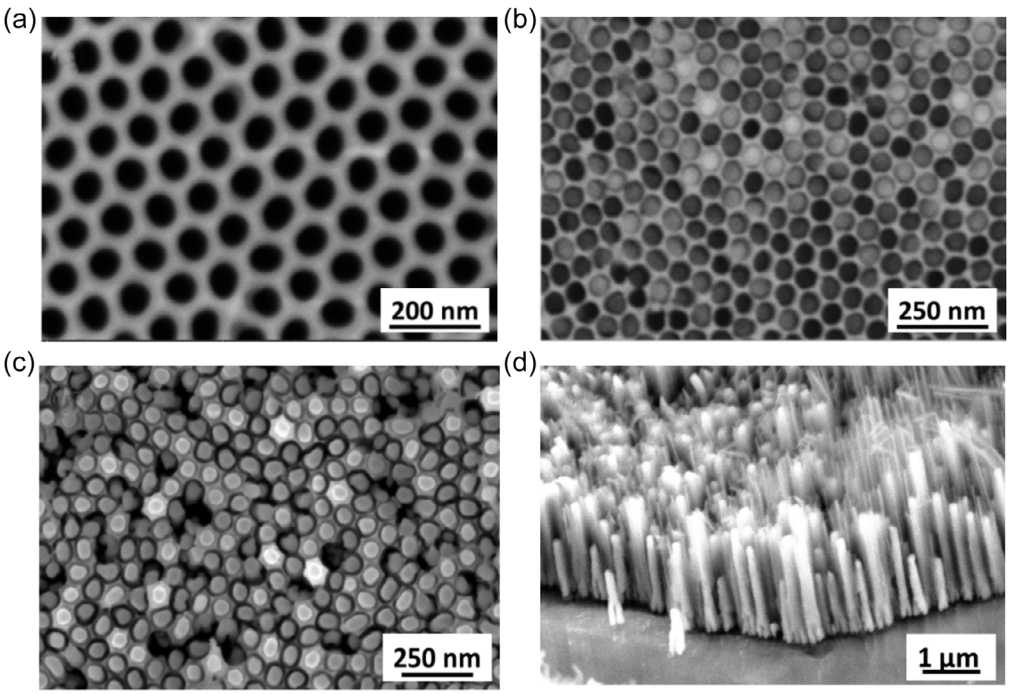

Figure 1. FESEM images of a) NAA substrate after 15 min pore widening and before nickel pulsed electrodeposition, b) surface image of NAA pores filled with nickel after pulsed electrodeposition, c) surface image of nickel nanorods inside the thin alumina pores, and d) cross-sectional image of nanorods with very thin alumina pore walls.

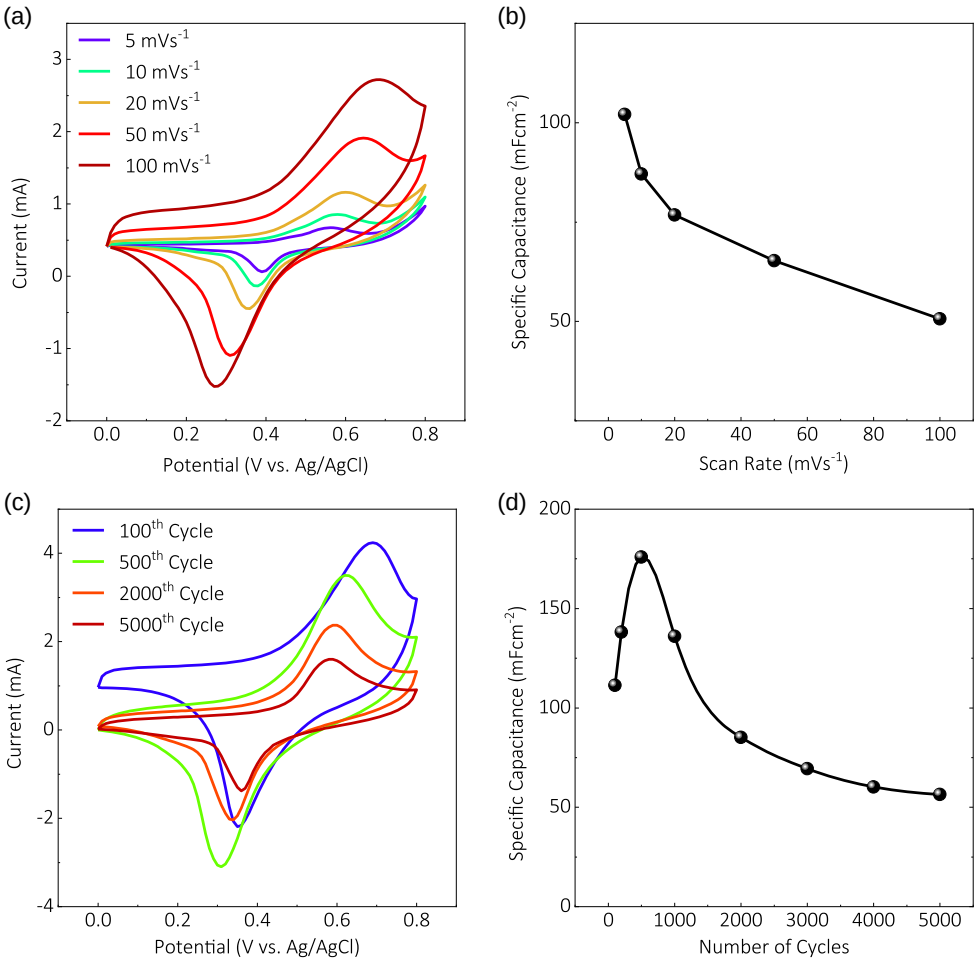

Figure 2. CV curve of Ni@NAA nanorods as working electrode with reference to Ag/AgCl reference in 1 M KOH solution: a) at different scan rates ranging from 5 to 100 mV s^{-1}, b) its corresponding specific capacitance, c) at different number of cycles (50 mV s^{-1}), and d) its corresponding specific capacitance.

KOH aqueous solution. **Figure 2**a displays the CV curves obtained at various scan rates ranging from 5 to 100 mVs^{-1}. The CV curves exhibit clear oxidation (anodic) and reduction (cathodic) peaks. The peaks shift symmetrically, and their maximum and minimum intensity increase with increasing scan rate, as expected in CV measurements.[26]

The specific capacitance of the Ni@NAA electrodes as a function of the scan rate is presented in the plot of Figure 2b. The value of C is estimated from the area within the CV curve as introduced for Equation (8) in the Experimental Section. The curve shows a decrease in specific capacitance with scan rate starting at a maximum of 102 mF cm^{-2} at 5 m V s^{-1}. The decrease is more pronounced at slow scan rates and stabilizes at higher scan rates with a minimum of 50 m Fcm^{-2} at 100 m V s^{-1}. The higher specific capacitances observed at low scan rates can be explained by the fact that slower scan rates allow longer times for ion diffusion through the electrolyte and accumulation on the electrode surface, resulting in higher charge values.

The CV curves of a Ni@NAA electrode, obtained at a scan rate of 50 mVs^{-1} after different number of cycles, are displayed in Figure 2c. The oxidation peak in the anodic part of the cycle occurs at a potential of about 0.64 V after 100 cycles and evolves until 0.55 V after 500 cycles. The reduction in the cathodic part of the cycle starts to occur at the potential of about 0.30 V and stabilizes around 0.38 V after 500 cycles. The CV curves for the initial cycles evolve toward lower currents: the maximum current for the 100th cycle is 4.45 mA while for 2000th cycle is 1.32 mA. After this, the maximum current remains almost stable. The minimum current exhibits a similar trend with a value of −2.1 mA for the 100th cycle and −1.94 mA for the 2000th cycle. Subsequently, the minimum current remains stable.

The first 100 voltage cycles are not shown in the figure as they do not result in closed CV curves. This can be related to the activation of the Ni@NAA samples with the creation of metal hydroxide species on the pure metal surface. The fact that CV measurements are not closed during the first 100 cycles indicates that nickel is being covered by more hydroxide at every cycle. Thus, closed CV curves can be an indication that all the nanorod surface is covered and that the electrochemical behavior is only related to both the redox reactions and to the diffusion of the redox species through the hydroxide layer. The anodic sweeps

of the CV curves exhibit certain asymmetry, suggesting partial irreversibility in the redox processes.

A graph of the specific capacitance as a function of the cycle number is shown in Figure 2d. Initially, after 500th cycling, the specific capacitance of the material increases. However, with subsequent cycles, the specific capacitance gradually begins to decrease. This initial increase phenomenon can be primarily attributed to an additional reactivation process undergone by the electrode material during the cycle test. Subsequently, the change in the rate of specific capacitance decrease can be linked to the growth of the nickel hydroxide layer within the Ni@NAA nanorods volume.[19] This growth implies an ionic conduction of OH^- species through the hydroxide layer, consequently the thicker the layer the more difficult for the hydroxide to grow, as indicated by the reaction provided in Equation (S1), Supporting Information). The decrease rate is 0.08 mF cm^{-2} per cycle during the initial phase, and then after the 500th cycle the specific capacitance started to decrease at 0.004 mF cm^{-2} per cycle at the end of the measurements, which indicates the transition to stability. At the 5000th cycle, the specific capacitance of the Ni@NAA electrode is 56 mF cm^{-2}, compared to 111 mF cm^{-2} at the 100th cycle. The specific capacitance retention of the Ni@NAA electrode was 78% after 5000th cycle (as compared to 2000th cycle), showing a high retention capacity of the electrode.

The samples were characterized via potentiostatic EIS measurements in the three-electrode configuration as a function of the voltage with respect to the Ag/AgCl reference electrode (see Figure S7, Supporting Information). The resulting EIS spectra in impedance (Z) Nyquist representation, i.e., the imaginary part ($''$) as a function of the real part ($'$), are shown in **Figure 3**a (dots). Several features can be observed. First, the higher the voltage, the smaller the resistance (R) at the lowest frequencies. This is evident when comparing the "semicircle radius" toward the right of the Z' axis of Figure 3a for the 0.8 V spectrum, with respect to those of the spectra below 0.6 V, which only show the beginning of "significantly larger semicircles." Moreover, toward high frequencies (left in the Z' axis of Figure 3a), two smaller resistances seem to be coupled with respective capacitances (C) which creates the overlapping of apparent semicircles in the Nyquist plots. Notably, these high-frequency RC couples do not appear to significantly change with bias voltage.

The capacitance from the EIS spectra can also be presented in Nyquist representation,[27] as shown in Figure 3b. Here, the definition of differential complex capacitance C^* is applied to relate the impedance with the capacitance:[28]

$$Z_C = \frac{1}{i2\pi f C^*} \tag{1}$$

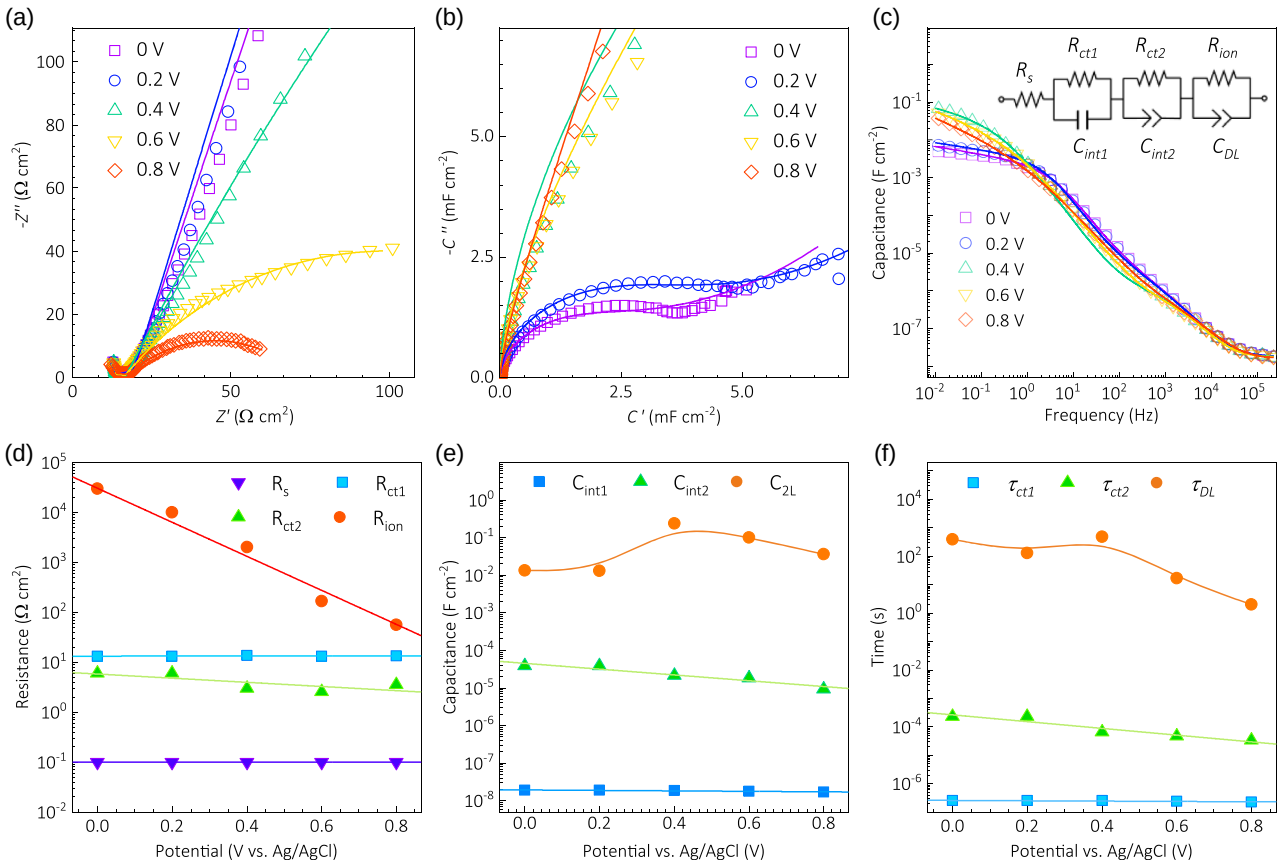

Figure 3. a–c) Impedance spectroscopy measurements and d–f) parameters obtained after fitting of an equivalent circuit model. The experimental (dots) and simulated (lines) spectra are shown in Nyquist representation for the impedance (a) and capacitance (b), and in Bode representation for capacitance (c). Using the equivalent circuit in the inset of (c) resulted in the resistance (d), capacitance (e), and response times (f), as indicated.

where i is the imaginary unit and f is the frequency of the perturbation. From Equation (1), $C^* = C' + iC''$ can be expressed as a function of the real and imaginary parts of impedance. Then, the imaginary capacitance results as

$$C'' = \frac{-Z'}{2\pi f(Z'^2 + Z''^2)} \tag{2}$$

and the real part of capacitance is

$$C' = \frac{-Z''}{2\pi f(Z'^2 + Z''^2)} \tag{3}$$

Similar to the impedance Nyquist plot, the capacitance Nyquist plot in Figure 3b shows that the smallest low-frequency capacitances appear in the range from units to tens of mF cm^{-2}. Moreover, the increase of capacitance with the applied voltage suggests a tradeoff between the resistance and the capacitance. This tradeoff reflects the chemical origin of the low-frequency capacitance which is enhanced as the current increases.

The capacitance is also plotted in Bode representation (as a function of the frequency) where the plateaus toward the lowest frequencies indicate the total capacitance and any intermediate plateau indicates independent capacitance signals. This is presented in Figure 3c, showing an uneven transition between what appears to be two plateaus at the lowest and highest frequencies. Toward higher frequencies, smaller charge transport capacitances may be the main contribution to the capacitance signal. These mechanisms are shown nearly independent on the applied voltage. On the other hand, toward lower frequencies, the higher capacitances depend on the bias and arise due to what can be assumed as double-layer capacitance and/or diffusion capacitance. Interestingly, with the increase of bias voltage, there is an increase of capacitance which appears to peak around 0.4 V before decreasing as the bias voltage is augmented.

The EIS experimental data were parameterized with the equivalent circuit schemed in the inset of Figure 3c. In addition to the series resistance (R_s), three RC couples were used in series for simulating the electrical response of the sample in alternating current mode. The first two Voigt elements were related to charge transport resistance (R_{ct1}, R_{ct2}) and interface capacitance (C_{int1}, C_{int2}), presumably at the electrodes. On the other hand, the third RC couple is related with the double layer and/or diffusion layer capacitance (C_{2L}) and the respective ion resistance (R_{ion}). The results of the equivalent circuit fittings are presented for the resistance, capacitance, and characteristic times $\tau = RC$ in Figure 3d,e,f, respectively. As suggested by the Nyquist plots in Figure 3a, the charge transport (high frequency) resistances behave constant or slightly linearly decreasing as the voltage bias increases. On the other hand, the ion-related (low-frequency) resistance shows an empirical exponential law as

$$R_{ion} = R_{ion0} \exp\left[-\frac{qV}{m_R k_B T}\right] \tag{4}$$

where $k_B T/q$ is the thermal voltage; R_{ion0} is the equilibrium resistance (at $V = 0$ V), and m_R is a voltage divisor coefficient. Particularly, $R_{ion0} \approx 30.4\ \text{k}\Omega\,\text{cm}^2$ and $m_R \approx 51$ for the studied sample. Furthermore, the capacitance fitting values are presented in Figure 3e. Similar to the resistance, the interface (high-frequency) capacitances C_{int1} and C_{int2} behave nearly constant (≈19 nF cm^{-2}) and linearly decreasing (9–38 μF cm^{-2}), respectively. Notably, C_{int1} was simulated as a "pure" capacitor, whereas a constant phase element (CPE) was employed for C_{int2}. The impedance of a CPE is

$$Z_{CPE} = \frac{1}{Y_{CPE}(i2\pi f)^p} \tag{5}$$

where Y_{CPE} (units of F cm^{-2} s^{p-1}) is the magnitude coefficient and p is the power of the CPE. The value of p indicates a "pure" capacitor ($Z_{CPE} = Z_C$) when $p = 1$, and hence $Y_{CPE} = C$, or a Warburg diffusion element when $p = 0.5$. Then, the characteristic response time of the CPE depends on the resistor in parallel, or series, as

$$\tau_{CPE} = (Y_{CPE} R)^{1/p} \tag{6}$$

and the effective capacitance, or pseudocapacitance, comes after

$$C_{CPE} = \frac{(Y_{CPE} R)^{1/p}}{R} \tag{7}$$

In the case of C_{int2}, $p \approx 0.5$ was found in the range of explored voltages, meaning that the decreasing behavior of the effective capacitance could be mostly due to the decrease of the coupled resistance R_{ct2} and diffusion charge transport phenomena. In the case of low-frequency C_{DL} values, the use of CPE circuit elements and the capacitance definition of Equation (7) were also needed. These are shown in Figure 3e as the highest estimated capacitances ranging from to 239 mF cm^{-2}. Similar to the capacitance behavior displayed in Figure 3c, $C_{DL} \approx 12$ mF cm^{-2} is minimum in equilibrium ($V = 0$ V), peaks maximum $C_{DL} \approx 239$ mF cm^{-2} around 0.6 V, and then decreases again as the voltage growths up to 0.8 V. This suggests that the electrochemical reactions producing the pseudocapacitance may be maximum around 0.6 V.

Last but not least, Figure 3f illustrates the characteristic response times resulting from the RC couples. These τ values illustrate the effective charging/discharging times for each Voigt element. In the case of high-frequency charge transport times, τ_{ct1} and τ_{DL} behave nearly constant (≈230 ns) and linearly decreasing (33–230 μs) as the voltage increases. On the other hand, the low-frequency values of τ_{DL} seem to saturate around ≈400 s before decreasing as the bias approaches 0.8 V.

All in all, the EIS analysis demonstrates the maximum differential capacitances of ≈200 mF cm^{-2} for operation at ≈0.4 V (vs Ag AgCl^{-1} electrode), which correspond to maximum charging times of ≈8 min. This behavior is shown to be very sensitive to the bias range, mostly due to the resistance dependency.

3. Conclusions

We have demonstrated the preparation of nanostructured Ni electrodes using NAA as template. The procedure permits to obtain arrays of Ni nanorods (Ni@NAA) embedded in the porous oxide matrix and with electrical contact with the aluminum substrate. The rods are separated an average distance of 90 nm, with an average diameter of 70 nm and an average length of 2 μm. The Ni nanorods and the porous oxide are separated by a space that

can be infiltrated by the electrolyte, permitting the formation of an electrochemical double layer and the realization of faradaic reactions between the electrode and the electrolyte ions.

CV measurements demonstrate a stable electrochemical behavior of the Ni@NAA after conducting 5000 cycles at a scan rate of 50 mVs^{-1}. Notably, specific capacitance shows an increase within the first 1000 cycles which can be related to the activation of the surface by the formation of Ni hydroxide. The Ni@NAA nanorod electrodes, with their enlarged active area and exceptional electrochemical performance, exhibit remarkable stability over long periods of use. Good agreement is demonstrated between the specific and differential capacitance from CV and EIS, respectively, both reporting maximum values above 100 mF cm^{-2}. In addition, the characteristic response time from EIS suggests maximum charging times of less than 10 min for the device operation. The obtained electrodes may represent a well-suited alternative for prospective applications in high-power energy devices that require pseudo-supercapacitance.

4. Experimental Section

Materials and Chemicals: Aluminum sheets of high purity (99.999%, 0.5 mm thickness) were purchased from Goodfellow, UK. Oxalic acid ($C_2H_2O_4{\cdot}2H_2O$), phosphoric acid (H_3PO_4), chromic acid (H_2CrO_4), nickel sulfate ($NiSO_4{\cdot}6H_2O$), nickel chloride ($NiCl_2{\cdot}6H_2O$), boric acid (H_3BO_3), and potassium hydroxide (KOH) were obtained from Sigma–Aldrich, UK. Deionized water was obtained from Elga purelab chorus system (Elga Labwater Corp., UK, 18.2 MΩ cm).

Nanostructured Electrode Fabrication: The aluminum substrates cut into 2 cm × 2 cm pieces were used for a commonly adopted two-step anodization procedure to achieve nanoporous anodic alumina.[20–22] The procedure involved using a 0.3 M oxalic acid solution at a temperature of 5 °C at an anodization voltage of 40 V. This results in a nanoporous oxide membrane with barrier oxide layer at the base of the pores, with a thickness ranging from around 40–50 nanometers. It is essential to remove such barrier layer at the bottom of the pores to establish an electrical pathway between the aluminum substrate and the inner pore volume.[23] This was achieved by implementing the step-down voltage reduction technique as described in by Nielsch et al. in 2000.[24] This approach involves a step-by-step decrease of the anodization current. At each step, current is instantaneously decreased by a constant factor which then causes anodization potential to decrease gradually until it stabilizes, at this moment the next current decrease step is applied. The steps are applied until a potential between 6 and 7 V is reached. As the potential is directly related with the barrier layer thickness, this process ends with a residual barrier layer of less than 10 nanometers. Further reduction of the potential could cause the oxide structure to completely peel-off from the aluminum substrate. This residual barrier layer was removed by immersing the substrate into a 5 wt% H_3PO_4 solution at 35 °C for 15 min (which simultaneously cause the widening of pore diameter also, see Figure S1, Supporting Information). For the nickel pulsed electrodeposition, the obtained NAA was set up as a working electrode in an electrochemical cell, whereas platinum served as the counter electrode. The electrolyte consisted of 8:4:1 weight ratio of nickel sulfate, nickel chloride, and boric acid (used as buffer) diluted in deionized water with pH maintained at 4.5 by adding KOH.[25] The electrolyte was kept at a constant temperature of ≈25–27 °C during the deposition procedure as described in ref. [21]. The controlled deposition was carried out to fill the length of the pores. Finally, the nickel deposited samples were immersed in a 5 wt% phosphoric acid solution at 35 °C for a short time of 5 min, with the objective of partially dissolving the alumina pore walls. This pore wall thinning process provides a space for the electrolyte to fill between the nickel and the aluminum oxide while at the same time maintains mechanical integrity of the Ni nanorods and ensures their electrical contact with the substrate.

Structural and Electrochemical Characterization: The obtained nanostructured nickel electrodes (Ni@NAA) were examined using FESEM (JEOL F200), CV, and EIS. The electrochemical cell used for electrochemical characterization consisted of a normal three-electrode setup. This setup included an Ag/AgCl electrode as the reference electrode, a Pt spiral wire as the counter-electrode, and the Ni@NAA as the working electrode. The electrochemical analysis was conducted in a 1 M KOH electrolyte solution at room temperature using an Ivium potentiostat (sModule 2.5 A 10 V^{-1}) operated with Iviumsoft software. The specific capacitance was calculated by the equation described as follows

$$C = \frac{A_c}{2k\Delta V a_s} \tag{8}$$

where C is the specific capacitance (F cm^{-2}), A_c is the power 'area' (W) enclosed in the CV curve, k is the scan rate (V s^{-1}), ΔV is the potential (V) window of the CV measurement, and a_s is the surface area (cm^2) of the Ni@NAA sample exposed to the electrolyte.

Supporting Information

Supporting Information is available from the Wiley Online Library or from the author.

Acknowledgements

O.A. acknowledges the Juan de la Cierva Fellowship grant FJC2021-046887-I funded by MICIU/AEI/10.13039/501100011033 and by the European Union NextGenerationEU/PRTR. T.A. acknowledges the predoctoral grant financially supported by the Agency for Management of University and Research Grants AGAUR-FI predoctoral program (2023 FI-00365) Joan Oró from the Secretaria d'Universitats i Recerca del Departament de Recerca i Universitats de la Generalitat de Catalunya and the European Social Plus Funds, and AGAUR-2021 SGR 00739 GRC Grant. This project has also received funding from the Spanish Ministerio de Ciencia e Innovación (MICINN) PDI2021-128342OB-I00, and by the Catalan Institution for Research and Advanced Studies (ICREA) under the ICREA Academia Award 2021. The authors also acknowledge the support of the NETPORE COST Action CA20126.

Conflict of Interest

The authors declare no conflict of interest.

Data Availability Statement

The data that support the findings of this study are available from the corresponding author upon reasonable request.

Keywords

cyclic voltammetry, electrochemical impedance spectroscopy, energy storage devices, pseudocapacitor, pulsed electrodeposition

Received: April 24, 2024
Revised: May 21, 2024
Published online: June 2, 2024

[1] R. Kötz, M. Carlen, *Electrochim. Acta* **2000**, *45*, 2483.
[2] W. G. Pell, B. E. Conway, *J. Power Sources* **2001**, *96*, 57.

[3] H. Ji, X. Zhao, Z. Qiao, J. Jung, Y. Zhu, Y. Lu, L. L. Zhang, A. H. MacDonald, R. S. Ruoff, *Nat. Commun.* **2014**, *5*, 3317.
[4] Z. Liu, X. Yuan, S. Zhang, J. Wang, Q. Huang, N. Yu, Y. Zhu, L. Fu, F. Wang, Y. Chen, Y. Wu, *NPG Asia Mater.* **2019**, *11*, 12.
[5] R. Reece, C. Lekakou, P. A. Smith, *ACS Appl. Mater. Interfaces* **2020**, *12*, 25683.
[6] J. Libich, J. Maca, J. Vondrak, O. Cech, M. Sedlarikova, *J. Energy Storage* **2018**, *17*, 224.
[7] G. Yao, N. Zhang, Y. Zhang, T. Zhou, *J. Nanopart. Res.* **2021**, *23*, 57.
[8] L. Fekri Aval, M. Ghoranneviss, G. Behzadi Pour, *Heliyon* **2018**, *4*, e00862.
[9] M. Iqbal, N. G. Saykar, A. Arya, I. Banerjee, P. S. Alegaonkar, S. K. Mahapatra, *J. Alloys Compounds* **2021**, *883*, 160705.
[10] A. K. Thakur, R. Bilash Choudhary, *Synth. Met.* **2016**, *220*, 25.
[11] X. Xiong, J. Chen, D. Zhang, A. Li, J. Zhang, X. Zeng, *Electrochim. Acta* **2019**, *299*, 298.
[12] K. K. Patel, T. Singhal, V. Pandey, T. P. Sumangala, M. S. Sreekanth, *J. Energy Storage* **2021**, *44*, 103366.
[13] Z. Ren, J. Li, Y. Ren, S. Wang, Y. Qiu, J. Yu, *Sci. Rep.* **2016**, *6*, 20021.
[14] R. Bolagam, S. Um, *Coatings* **2020**, *10*, 200.
[15] C. Ji-Hyun, K. Su-Jeong, S. Jung, J. Duk-Young, *ACS Appl. Energy Mater.* **2020**, *3*, 3854.
[16] Y. Lei, B. Daffos, P. L. Taberna, P. Simon, F. Favier, *Electrochim. Acta* **2010**, *55*, 7454.
[17] A. M. Abdalla, R. P. Sahu, C. J. Wallar, R. Chen, I. Zhitomirsky, I. K. Puri, *Nanotechnology* **2017**, *28*, 075603.
[18] W. Mao-Sung, H. Yu-An, Y. Chung-Hsien, *J. Electrochem. Soc.* **2008**, *155*, A798.
[19] L. Gu, Y. Wang, R. Lu, L. Guan, X. Peng, J. Sha, *J. Mater. Chem. A* **2014**, *2*, 7161.
[20] H. Masuda, K. Fukuda, *Science* **1995**, *268*, 1466.
[21] A. Santos, L. Vojkuvka, M. Alba, V. S. Balderrama, J. Ferre-Borrull, J. Pallares, L. F. Marsal, *Phys. Status Solidi A* **2012**, *209*, 2045.
[22] A. Santos, J. Ferré-Borrull, J. Pallarès, L. F. Marsal, *Phys. Status Solidi A* **2011**, *208*, 668.
[23] A. Santos, L. Vojkuvka, J. Pallarés, J. Ferré-Borrull, L. F. Marsal, *J. Electroanalytical Chem.* **2009**, *632*, 139.
[24] K. Nielsch, F. Müller, A. P. Li, U. Gösele, *Adv. Mater.* **2000**, *12*, 582.
[25] A. Santos, L. Vojkuvka, J. Pallarés, J. Ferré-Borrull, L. F. Marsal, *Nanoscale Res. Lett.* **2009**, *4*, 1021.
[26] N. Elgrishi, K. J. Rountree, B. D. McCarthy, E. S. Rountree, T. T. Eisenhart, J. L. Dempsey, *J. Chem. Educ.* **2018**, *95*, 197.
[27] H. Bechert, O. Almora, K. Regau, G. J. Matt, C. J. Brabec, T. Wehlus, *Adv. Mater. Technol.* **2019**, *4*, 1800696.
[28] J. Bisquert, F. Fabregat-Santiago, in *Dye-Sensitized Solar Cells* (Ed: K. Kalyanasundaram), CRC Press, Lausanne (Switzerland) **2010**, p. 457.